GEOPHYSICS, VOL. 86, NO. 3 (MAY-JUNE 2021); P. B193–B207, 19 FIGS., 3 TABLES.
10.1190/GEO2020-0294.1

Tube-wave monitoring as a method to detect shear modulus changes around boreholes: A case study

Daniel Wehner[1], Filipe Borges[2], and Martin Landrø[3]

ABSTRACT

Monitoring the shear modulus of formations around boreholes is of interest for various applications, ranging from near-surface investigation to reservoir monitoring. Downhole logging tools and borehole seismic are common techniques applied to measure and characterize formation properties. These methods rely on transmitted and reflected waves to retrieve the rock properties. Wave modes traveling along the interface between the well and the formation, such as tube waves, are often considered as noise. However, tube waves are less attenuated than body waves and contain information about the shear modulus of the formation surrounding the well. Hence, a potential use of this interface wave is of interest. Because tube-wave properties depend on several parameters, e.g., well geometry, highly accurate measurements should be performed for use in inferring rock properties. We have studied the feasibility of tube-wave measurements as a monitoring method. Different experiments are conducted using a hydrophone array in two boreholes, with depths of 30 and 95 m. The experiments are used to investigate how accurately the tube-wave velocity can be measured and which parameters have the most impact on the measurements. Our results suggest that it is hard to estimate the absolute shear modulus of the geologic formation using tube-wave velocities only. However, it seems feasible to use them to monitor changes in the shear modulus, depending on the borehole setup and the geologic formation. Tube-wave monitoring can be used as a first step to determine the depth along the well where changes occur before more accurate measurements are performed in a second step.

INTRODUCTION

Estimating and monitoring the soil and rock formation properties around boreholes plays an important role in engineering and exploration activities. In near-surface applications, subsurface monitoring is relevant for foundations at large construction sites, as well as for observing environmental changes. Deeper objectives for monitoring are subsurface energy storage sites for compressed air or gas, used to fill gaps of energy supply from renewable sources. Another activity in which subsurface monitoring is required is carbon capture and storage, widely regarded as being crucial to achieve the CO_2 emission goals — especially from CO_2-intensive industrial enterprises such as cement and fertilizer factories or recycling plants (Ringrose, 2017). Because storage facilities must prevent any leakages from deep sites into shallower geologic layers, accurate knowledge of the geology and formation changes is desired. In general, an optimal monitoring technique should be robust, accurate, and economically feasible, and it should record data within a reasonable time and spatial samplings.

Borehole geophysical measurements are often used to image the subsurface and detect potential changes. Seismic methods are one of the most commonly applied techniques. Most seismic monitoring techniques make use of reflected or transmitted body waves, for instance, vertical seismic profiling (VSP). When acquiring seismic data in boreholes, interface waves between the well and the geologic formations are also recorded. These interface waves are often referred to as tube waves (Galperin, 1985), and they are mostly considered as noise in VSP measurements. For acoustic well logging,

Manuscript received by the Editor 6 May 2020; revised manuscript received 10 January 2021; published ahead of production 10 February 2021; published online 21 April 2021.
[1]NTNU, Department of Geoscience and Petroleum, Trondheim 7031, Norway and EGEOS GmbH, Kiel 24118, Germany. E-mail: daniel.wehner@t-online.de (corresponding author).
[2]NTNU, Department of Geoscience and Petroleum, Trondheim 7031, Norway and Petróleo Brasileiro S/A (Petrobras), Rio de Janeiro 20031-912, Brazil. E-mail: filipeborges@petrobras.com.br.
[3]NTNU, Department of Electronic Systems, Trondheim 7491, Norway. E-mail: martin.landro@ntnu.no.

DOI:10.1190/geo2020-0294.1

there are patents on systems and methods to extract information from tube waves (Overton, 1957; Ferre, 1960; Stevens and Day, 1986). In addition, there are studies showing how the tube wave might be used to retrieve information about permeability when the borehole fluid is coupled to porous and permeable rock formations (White, 1965; Chang et al., 1988; Winkler et al., 1989).

In general, the propagation velocity of the tube wave is linked to the shear modulus of the surrounding rocks (White, 1965; Carcione and Poletto, 2008). Therefore, shear modulus variations might be estimated by measuring the tube-wave velocity. If such information can be extracted from the tube wave, this technique would have some advantages over conventional VSP measurements. It would be sensitive only to the shear modulus of the formation surrounding the borehole, whereas traveltimes and amplitudes of P- and S-waves also depend on other parameters, for instance, density. Furthermore, tube-wave monitoring only requires a hydrophone array or fiber-optic cable within the well and one stationary source. Potentially, passive recordings might be sufficient to detect changes. The receivers could then be deployed as a cheap, permanent surveillance system at specific monitoring sites.

For near-surface applications, shear modulus changes can occur due to several mechanisms, such as variations in the stress environment, aging effects in the soil (Troncoso and Garcés, 2000), or load at solid waste disposal sites (Dixon et al., 2005). Henriet et al. (1983) show how tube waves could be used for near-surface investigations for a dam site. For offshore operations such as the construction of wind turbine foundations or overburden monitoring at reservoirs sites, the S-wave velocity is often retrieved from Scholte surface waves by active (Kugler et al., 2005, 2007) or passive (Bussat and Kugler, 2011; De Ridder and Biondi, 2015) measurements. Mordret et al. (2014) present a field example for monitoring the reservoir overburden using noise recordings. The tube wave could then be used as a complementary tool to these measurements, when wells are available in the area. The well measurements could improve the depth information of the estimated S-wave velocities from surface measurements.

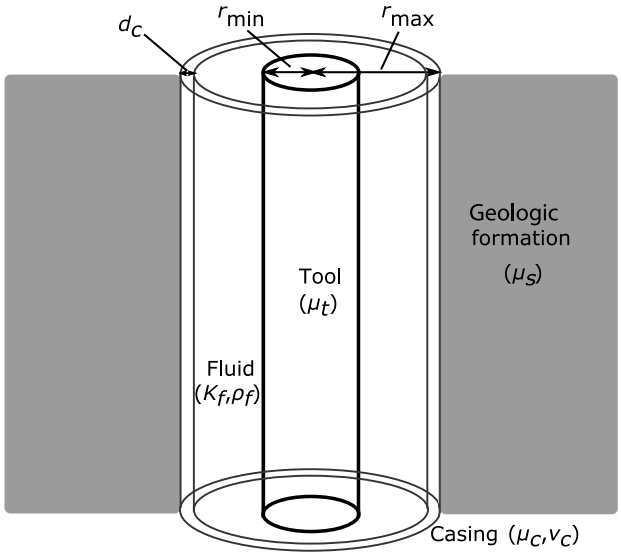

Figure 1. Borehole setup and the important parameters for the relation between the tube wave and shear modulus μ_S within the geologic formation. The terms K_f and ρ_f are the bulk modulus and density of the borehole fluid, respectively, μ_t is the shear modulus of the tool, and μ_c and ν_c are the shear modulus and Poisson's ratio of the casing, respectively.

We investigate the potential use of tube waves as a monitoring tool that detects variations of the shear modulus in the geologic formation surrounding wells. Because the tube-wave velocity depends on several parameters other than the formation shear modulus, the main question is: how precisely can rock properties be estimated from tube-wave measurements? To examine that, we conduct experiments within a 30 and 95 m deep borehole to check how accurately the tube-wave velocity can be measured. Experiments with an active source and with noise recordings are performed, and we discuss the various factors that impact our measurements, as well as the sensitivity of the results to these factors. Different numerical approaches to compute the tube-wave velocity are compared. The experimental results should indicate whether tube-wave measurements can be used as a monitoring method and which borehole and geologic settings are beneficial.

THEORY

Two important points are described within this section. First, the relation between the tube-wave velocity and the shear modulus of the formation surrounding the borehole is explained. Second, the methods used to estimate the tube-wave velocity from seismic measurements are described.

Relation between the tube wave and the shear modulus

A wave that propagates on the interface between two media is referred to as an interface or surface wave. Surface waves are labeled according to the interface along which they propagate, as well as the propagation mode, e.g., Rayleigh waves in solid-vacuum interfaces (Rayleigh, 1885), Scholte waves in solid-fluid interfaces (Scholte, 1942, 1947), and Stoneley waves in a solid-solid interface (Stoneley, 1924). In the specific case of boreholes, Stoneley waves appear at the interface between the casing and the cement layer, as well as between the cement and the formation. These interface waves are often referred to as tube waves (Galperin, 1985). Tube waves are usually generated at the wellhead, at shear zones, or at fractures close to the well, by a squeeze effect of incident P-, S-, and Rayleigh waves (Hardage, 1981; Peng et al., 1996). In this work, we focus on tube waves as first derived by Biot (1952) that are a low-frequency approximation of the exact dispersion relation, also presented by Norris (1987) as a particular case of Biot's slow wave for a cylindrical-shaped pore.

The relation between the tube wave and the shear modulus within the formation depends on several parameters of the well materials and geometry. To illustrate the important parameters, a sketch of a borehole is shown in Figure 1. The cylindrical tool inside the well could be a measuring tool or an injection pipe.

A detailed explanation of the relation between tube-wave velocity and formation shear modulus can be found in Schoenberg et al. (1981) and Marzetta and Schoenberg (1985). For the tube-wave velocity within an open borehole (no casing), including a tool, the relation is

$$v_{t_1} = \left\{ \rho_f \left[\frac{1}{K_f} + \frac{1}{1-\eta} \left(\frac{1}{\mu_S} + \frac{\eta}{\mu_t} \right) \right] \right\}^{-1/2}, \qquad (1)$$

DOI:10.1190/geo2020-0294.1

where ρ_f and K_f are the density and bulk modulus of the borehole fluid, respectively, μ_t is the shear modulus of the tool, μ_S is the shear modulus of the geologic formation, and $\eta = r_{min}^2/r_{max}^2$ is a geometric factor depending on the different radii (Figure 1). If the borehole is cased and no tool is deployed inside it, the tube-wave velocity is (Norris, 1990)

$$v_{t_2} = \left\{\rho_f\left[\frac{1}{K_f} + \frac{1}{N}\right]\right\}^{-1/2}, \tag{2}$$

where

$$N = \frac{2(1-\nu_c)\mu_S + (\mu_c - \mu_S)(1-a^2)(1-\beta\nu_c^2)}{2(1-\nu_c) - (1-\mu_S/\mu_c)(1-2\nu_c+\beta\nu_c^2)(1-a^2)}, \tag{3}$$

and ν_c and μ_c are the Poisson's ratio and shear modulus of the casing, respectively, and $a = (r_{max} - d_c)/r_{max}$ is another geometric factor, also depending on the casing thickness d_c. The parameter β defines the coupling between the casing and the formation where $\beta = 1$ allows for movement of the casing in the axial direction relative to the formation, whereas $\beta = 0$ restricts this movement. Finally, for a cased borehole with a tool inside, the tube-wave velocity is (Norris, 1990)

$$v_{t_3} = \left\{\rho_f\left[\frac{1}{K_f} + \frac{\eta}{(1-\eta)\mu_t} + \frac{1}{(1-\eta)N}\right]\right\}^{-1/2}. \tag{4}$$

It is interesting to note that the tube-wave velocity is a function of the shear modulus μ_S of the formation, and not of its density. Therefore, density changes within the formation caused by fluid substitutions or other mechanisms are not expected to cause changes in the tube-wave velocity. Although shear strength commonly correlates with density, that correlation is usually linked to different mineralogy, diagenesis, and pore structure: once the rock frame is fixed, most common poroelastic models (Biot, 1941) predict no change in shear modulus under different pore fluid contents, even if the density changes. For example, under Gassmann's equations (Gassmann, 1951), a fluid substitution that does not change the rock frame would change the formation's S-wave velocity, but not the tube-wave velocity measured in the well. This would be valid if assumptions such as linear elasticity and pore pressure equalization hold, which might not always be the case.

The dependence of the tube wave on the shear modulus and the S-wave velocity of the formation is illustrated in Figure 2; the relation for open and cased boreholes is also illustrated by Carcione and Poletto (2008). For this example, parameters similar to that of our experimental setup are chosen: $\rho_f = 1000$ kg/m^3, $K_f = 2.15$ GPa, $\nu_c = 0.25$, $\mu_c = 78$ GPa, $\mu_t = 1$ GPa, $r_{min} = 0.02$ m, $r_{max} = 0.15$ m, and $d_c = 0.005$ m. To estimate the S-wave velocity, we assume a density of $\rho_s = 2000$ kg/m^3 for the formation. For this example, the movement of the casing is allowed ($\beta = 1$). Because the goal is to use the tube-wave velocity as a monitoring method, a steeper curve for $v_t(\mu_S)$ is desirable because small changes in the shear modulus would lead to significant variations in the tube-wave velocity.

Tube-wave velocity estimation

Equations 1, 2 and 4 are low-frequency approximations of the dispersion relation for wave modes propagating at the interface between the well and the formation, presented by Marzetta and Schoenberg (1985). The modeled dispersion relations for parameters similar to the ones in our experimental setup indicate that, for the frequency range examined in the experiments (<500 Hz), the events are virtually nondispersive. This is valid for an open and cased borehole. The relative difference between the low-frequency approximation and the exact dispersion relation is less than 0.0025%. If there is little or negligible dispersion, the expected behavior of the event in the f-k domain is a straight line. The group velocity of an event can be calculated as df/dk, where f is the frequency and k is the wavenumber. Therefore, this group velocity can be estimated as the angular coefficient of a line in the f-k Fourier plot. Here, we propose two methods for obtaining the angular coefficient of this line.

Least-squares line fit

The first method used to estimate the velocity is a least-squares line fit through the maxima in the f-k domain. Then, the tube-wave velocity v_t is estimated as

$$v_t = \arg\min \sum_i |f_i - \alpha k_i^{max}|^2, \tag{5}$$

where α is an angular coefficient. The core idea of the method is that, for every frequency f_i in a 2D Fourier plot, the wavenumber k_i^{max} of the maximum amplitude is picked. After that, the line going

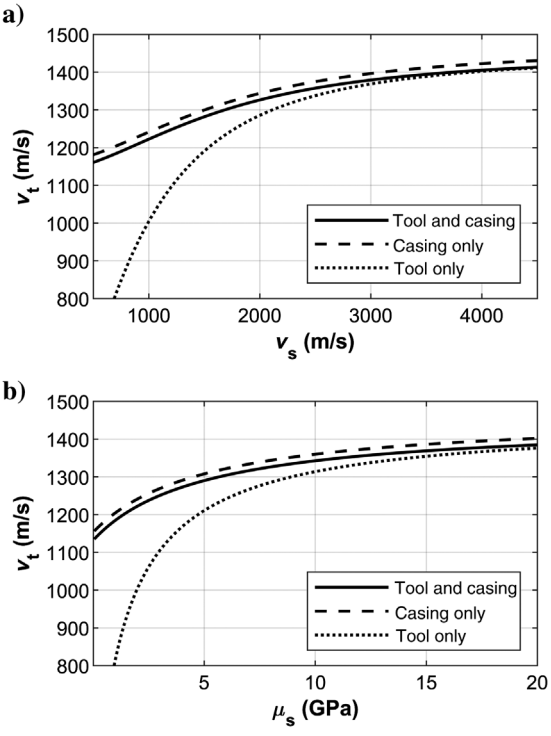

Figure 2. Relation between the tube-wave velocity v_t and (a) S-wave velocity V_S and (b) shear modulus μ_S within the formation surrounding the well, for different settings.

through the origin that has the smallest least-squares differences to those points is selected as the best fit. The angular coefficient α of the best-fit line is a good approximation for df/dk, and it can be interpreted as the velocity v_t of the nondispersive event.

Figure 3 shows a simple sketch of a linear event observed in the f-k domain where the dark colors represent stronger amplitudes. The blue dots illustrate the maximum amplitudes that are picked, and the red y axis represents the best least-squares fit to all points that go through the origin. The tube-wave velocity is represented with the angular coefficient $\alpha = \tan\theta$.

Radon transform

Given the linear nature of the events that are measured, another method of particular interest is the linear Radon transform (Radon, 1986), also known as the τ-p transform (Claerbout, 1985). The Radon transform $R(x',\psi)$ of a 2D function $F(x,y) = F(\mathbf{r})$ is the line integral of F on the lines L and can be written as

$$R(x',\psi) = \int_L F(\mathbf{r})|d\mathbf{r}| \quad \text{or}$$
$$= \int_{-\infty}^{\infty} F(x'\cos\psi - y'\sin\psi, x'\sin\psi + y'\cos\psi)dy', \tag{6}$$

where x' and y' are the rotated axes of the coordinate system and ψ is the rotation angle with respect to the f-k domain (Figure 3).

As discussed previously, the tube wave measured in our experiment is expected to be mapped as a linear event in the frequency-wavenumber domain. By calculating the line integral for several angles ψ in the 2D Fourier plot, the resulting transform would have its maximum when the line integral is performed along a path that has the same inclination as the tube-wave event. The geometry of Figure 3 shows that the focusing of the Radon integral occurs at an angle $\theta = \psi + 90°$. As the event goes through (0m^{-1}, 0 Hz), the maximum for the example in Figure 3 appears at a displacement $x' = 0$ (the Radon transform is calculated assuming the f-k transform as an image; hence, x' is dimensionless, being measured in pixels). We note that the Radon transform and the line-fit method should theoretically lead to the same result for v_t.

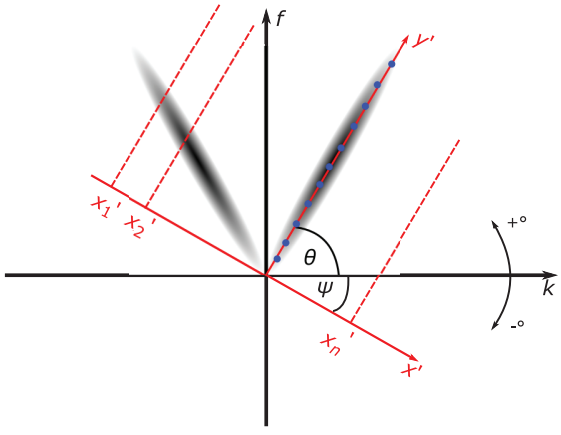

Figure 3. Simple sketch of a linear symmetric event in the f-k domain indicated by the dark ellipses. The blue dots denote the maximum amplitudes picked for the line fit, and θ is the angle between the fitted line and the k axis. The red coordinate system represents the Radon transform rotated by an angle ψ. The dashed red lines illustrate the series of line integrals performed parallel to the axis y'. The values of these integrals represent $R(x',\psi)$. Note that the angle θ is positive, whereas ψ is negative as indicated by the black arrow.

EXPERIMENTS

The experiments are conducted within two boreholes located inside a work hall. The setup is shown in Figure 4. The wells were drilled to different depths and have different diameters. We call the shallow borehole (depth of 30 m) well 1 and the deep borehole (depth of 95 m) well 2. Both wells are lined with a steel casing made of steel type S355J2H, commonly used in pipe constructions. The casing of well 2 is thicker than the one used in well 1. No cementing has been used between the casing and the formation. The parameters are summarized in Table 1. Both wells are filled with water, and the water table is shown as the dashed line in Figure 4.

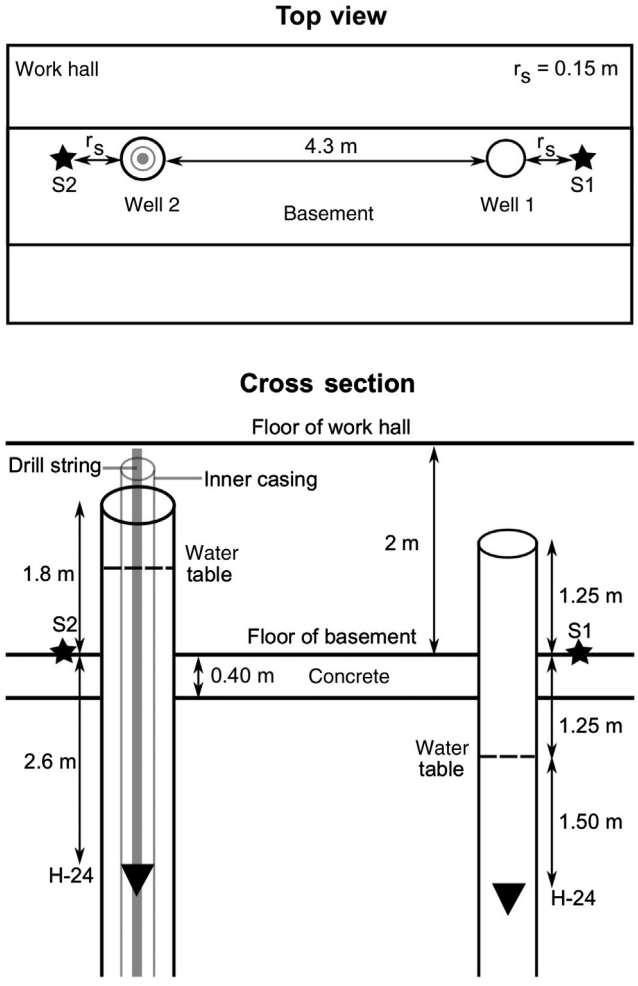

Figure 4. Experimental setup inside the work hall. Wells 1 (30 m deep) and 2 (95 m deep) are shown in top view and cross section. The stars indicate the positions of the hammer source. The shallowest hydrophone is indicated by H-24, with a regular spacing of 1 m to the next receivers. The drill string and inner casing (light gray) are only temporarily installed for one set of experiments, the semipassive experiment.

DOI:10.1190/geo2020-0294.1

The deep well is filled with tap water because it is plugged with cement at the bottom of the well. In contrast, the shallow well is open at the bottom, and its filling fluid contains more minerals dissolved from the formation water. The water temperature in the deep well varies between $T_w = 10$°C at the top to $T_w = 7$°C at the bottom. In the shallow well, the temperature ranges from $T_w = 13$°C at the top to $T_w = 8$°C at the bottom. For the model, we assume a mean temperature difference of 3°C between the borehole fluids. The density ρ_f and bulk modulus K_f of the filling fluid are estimated using the empirical relations from Batzle and Wang (1992). The results for ρ_f and K_f are given in Table 1. The estimated density values ρ_f fit with the pycnometer measurements conducted with samples from both wells.

For all recordings, the same 24-channel hydrophone array is used. The array consists of SQ54 hydrophones (Geotomographie GmbH) separated by 1 m, with a flat frequency response between 1 and 10 kHz, and it can be operated down to a depth of 500 m. The array contains a Kevlar tension string, and the cable is jacketed with a PVC coating. The shear modulus of the hydrophone array is set to the value for the PVC coating, and the radius $r_{\min}$ (Table 1) is estimated from the mean thickness of the individual hydrophones and the cable. It should be noted that precise knowledge of the array parameters is not relevant when monitoring applications are considered because the parameters of the tool are not expected to change during the measurements. The depths where the hydrophones are located are illustrated in Figure 4, with channel 24 being the shallowest receiver. The geology around the boreholes is expected to consist mostly of marine homogeneous clay sediments as seen from the X-ray diffraction analysis of the drilling material and the well logging that was done before the casing installation. The geology seems to be similar to the Eberg site (Long and Donohue, 2007), which is close to our experimental site.

Three different types of experiments are conducted: (1) active measurements with a hammer source, (2) a semipassive experiment in which a drill string in well 2 acts as a strong noise source, and (3) a passive experiment in which noise is recorded over a longer time period. These experiments are described in more detail as follows:

1) Active experiments: One experiment is conducted in well 2 in October 2017, and four experiments are conducted in well 1 in September 2017 (test 1), October 2017 (test 2), March 2018 (test 3), and May 2018 (test 4). In total, 80 hammer shots are performed for each test at the respective source location (S1 for well 1, S2 for well 2; see Figure 4). Noise recordings of 10 s are performed before and after each test (except for test 1). The total recording time for each record is $t_{\max} = 1$ s, and the sampling is $dt = 0.25$ ms. There are two main reasons for this experimental configuration. First, the tube-wave velocity can be investigated for two different borehole geometries, at almost the same geologic location. Second, the repeated tests can demonstrate the accuracy of the measurements because no changes in the formation surrounding the well are expected.
2) Semipassive experiment: The experiment is conducted in May 2018. The drill string in well 2 is active for approximately 76 s, whereas the hydrophone array in well 1 measures the signal in short time periods. The drill string is installed inside a second inner casing of well 2. During the operation, it is expected that the drill string hits the casing at different depth locations. The total recording time for each record is $t_{\max} = 4$ s, and the sampling is $dt = 0.25$ ms. More details about the experiment with the drill string are given by Wehner et al. (2018). The measurements are compared with the active experiments, and we investigate if a strong background source can replace the active source for measuring the tube wave with a high accuracy.
3) Passive experiments: The experiments are conducted in October 2017. The hydrophone array is first installed in well 1 and afterward in well 2. The background noise is continuously recorded for $t_{\max} = 11$ h. The sample rate for the measurements is $dt = 1$ ms. We investigate the accuracy of the measured tube-wave velocity from passive measurements and if long recording times lead to results that are comparable with the active measurements.

The comparison of all experiments should help us identify which acquisition methods might be useful for field applications.

RESULTS

We start this section by presenting the recorded seismic data from the experiments in both wells and proceed to estimate the tube-wave velocity for our experiments. Then, we estimate the shear modulus in the formation from the measured tube-wave velocity. Finally, we model the sensitivity of each single parameter that has an impact on the tube-wave velocity.

Recorded waves in boreholes

The first 50 ms of stacked recordings in one active experiment for wells 1 and 2 is shown in Figure 5. The hammer shots are not synchronized with the beginning of the recording; therefore, time zero does not correspond to the time when the hammer hits the floor. The recordings for both wells are aligned according to the first arrival. Three different coherent signals are highlighted by arrows in Figure 5. The arrivals indicated by the black arrows have a velocity of 5800 m/s, which matches the P-wave velocity of the steel

Table 1. Important parameters of the shallow well 1 and the deep well 2.

Borehole	Well 1	Well 2
Borehole parameters		
Radius ($r_{\max}$) (m)	0.075	0.15
Depth (z_w) (m)	30	95
Casing parameters		
Thickness (d_c) (m)	0.004	0.005
Poisson's ratio (ν_c)	0.26	0.26
Shear modulus (μ_c) (GPa)	78	78
Fluid parameters		
Density (ρ_f) (kg/m^3)	998.8	999.2
Bulk modulus (K_f) (GPa)	2.10	2.07
Temperature (T_w) (°C)	11	8
Hydrophone array parameters		
Radius ($r_{\min}$) (m)	0.013	0.013
Shear modulus (μ_t) (GPa)	1.0	1.0

casing. The arrivals marked by the blue arrows have a velocity of 1650 m/s and are assumed to be the direct P-wave that travels from the source to the receivers. The velocities of the casing wave and the P-wave are estimated by picking the amplitude peaks. The tube waves (the red arrows) arrive later because they are expected to have a velocity slower than 1500 m/s, which is the P-wave velocity of the borehole fluid.

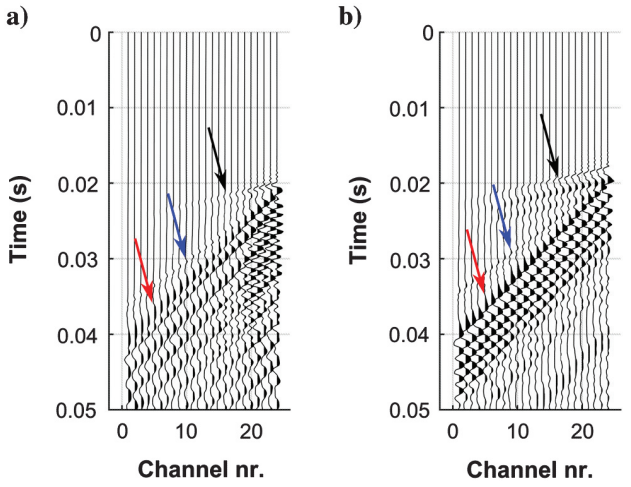

Figure 5. Stacked traces for an active experiment in (a) the shallow well 1 and (b) the deep well 2. An automatic gain control is applied to enhance the signal of the direct P-wave. The shallowest hydrophone (24) starts at approximately 3 m depth (Figure 4).

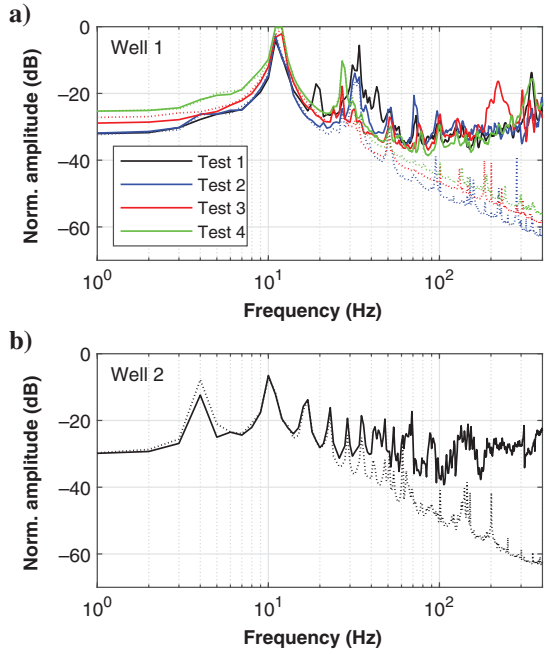

Figure 6. The solid lines are the smoothed, mean frequency spectra for a time window of 1 s of all shots of the active experiments in (a) well 1 and (b) well 2. The dotted lines illustrate the corresponding noise spectra before and after the experiment. The amplitudes are normalized to the maximum value of all recordings.

A ringing effect is recognized after the tube-wave arrival, being particularly strong at the shallowest receivers (20–24) of well 1 (Figure 5a). This ringing could be due to several tube waves, generated by P-, S-, and Rayleigh waves hitting the wellhead and well bottom, traveling simultaneously along the well. These reverberations happen in a short time period because the source is quite close to the well (Figure 4). Also due to the short distance between the well and the source, reflected waves from the wellhead arrive shortly after the first tube wave.

Figure 6 shows the frequency spectra for the active source and noise recordings. The spectra for the noise and the active source are nearly the same for frequencies below 40 Hz, where the amplitudes are stronger for all recordings. In well 1, the spectra for all tests are very similar for most frequency ranges, although the peak at approximately 30 Hz for the first two tests has slightly shifted to a lower frequency for the later tests 3 and 4. The frequency spectra of the deep well experiment have a slightly higher amplitude content for most frequencies compared to those of the shallow well, except for the peaks at approximately 10, 30, and 350 Hz in the shallow one. The deep well spectra reveal periodic peaks at different frequencies, which are also identified in the frequency spectra from passive recordings (Figure 7).

The passive measurements are recorded in single files with length of 16 s. For the shallow well, the periodic frequency peaks are approximately at 10, 30, 50, 70 Hz, etc. (Figure 7, the black line). For the deep well, peaks are approximately 3, 9, 15, 21, 27 Hz, etc. (Figure 7, the red line). These peaks can be interpreted as harmonics in the wells and hence depend on the depth of the borehole. The ratio z_{w1}/z_{w2} of the depths $z_{w1} = 30$ m and $z_{w2} = 95$ m for the shallow and deep wells, respectively, is 0.316, which is the same for the ratio of the frequency intervals (20 and 6 Hz) between the peaks in Figure 7.

It can be noted that, between October 2017 and March 2018, the general noise level in the shallow well varies for frequencies greater than 20 Hz and the periodic peaks are not as clear as previously. Other peaks, e.g., approximately 23 and 27 Hz, are present in all recordings and could be caused by the running engines of the ventilation and heating system in the work hall. This is reinforced by geophone noise recordings inside and outside the work hall, which confirm that these noise peaks are significantly reduced outside of the building. That could explain the shift appearing at approximately

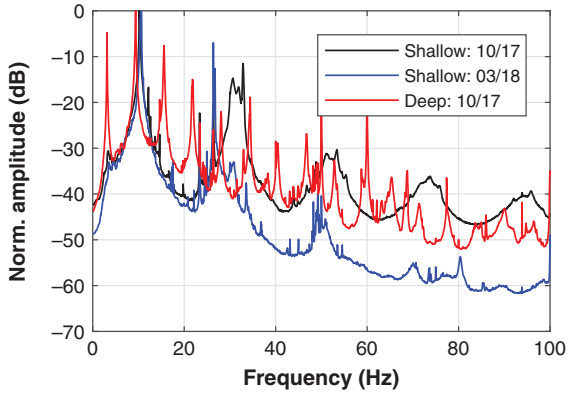

Figure 7. Smoothed, mean frequency spectra for time windows of 16 s of passive recordings in the shallow and deep wells at different times.

DOI:10.1190/geo2020-0294.1

30 Hz between tests 1 and 2 and tests 3 and 4 of the shallow well (Figure 6a) because the noise level in the work hall could have been different on the days of the data acquisition.

The data for both wells are filtered within different frequency bands, and the normalized stacked seismograms are shown in Figure 8. The cutoff frequencies of the band-pass filter in Figure 8a and 8c are chosen to remove the part where the noise and the active hammer shots have the same energy content (Figure 6). The frequencies greater than 450 Hz are removed to compare the plots to the analysis in the f-k domain that is performed later for the velocity estimation. As can be seen, most of the energy within this frequency range is related to the tube wave, which becomes clearer for frequencies below 150 Hz (Figure 8b and 8d). For well 1, the first downgoing and bottom-reflected tube wave can be recognized in Figure 8b, whereas the amplitudes of later reflected tube waves are more difficult to identify. In well 2, the first bottom-reflected tube wave can be identified starting at 0.16 s at receiver 1, accounting for the greater depth of this borehole (Figure 8d). The second downgoing tube wave is also visible, starting at 0.19 s at receiver 24.

Two main differences can be recognized between both wells. First, the fast casing wave at the beginning of the record is much stronger in the deep well (Figure 8c), which could be related to a better coupling between the formation and the casing in the deep well. This would explain the clear bottom reflection in the deep well because the intensity of the tube wave depends on this coupling (Galperin, 1985). Second, between the first downgoing and bottom-reflected tube wave in the deep well, several other up- and downgoing events can be recognized (Figure 8d). Because the casing has the same diameter all the way down to the bottom, these reflections could in principle be related to geologic interfaces within the formation. However, borehole logging during the well drilling did not indicate any strong interfaces. Another explanation could be a reflection from the end of the tool inside the borehole, which would fit to the timing of those reflections. In addition, the shallow well is very close (4.3 m apart, Figure 4), and the depth of that well has almost the same length as the hydrophone array. Therefore, the tube wave that travels along the shallow well might be measured in the deep well. This option is, however, less likely because the amplitude of this wave should be weaker when compared to that of the tube wave that travels along the deep well. Although the nature of these additional reflections is not fully explained, it is an advantage to have several tube waves traveling in the medium because this improves the results of our proposed velocity estimation method.

Tube-wave velocity estimation

The tube-wave velocity is computed in the f-k domain, representing an average velocity in the range of the receiver array. This proves to be a reliable technique for this purpose because the tube wave carries a lot of energy and it can travel the well up and down several times. The f-k panels of a single shot in wells 1 and 2 are shown in Figure 9. We notice a strong event, for the positive and negative wavenumbers, corresponding to the down- and upgoing tube wave, respectively. The higher energy content in the deep well is clearly visible in these plots. The stronger casing wave in the deep well can be identified as a steeper event (Figure 9b).

As previously mentioned, the velocity of the tube wave is estimated by two methods. The first one is the least-squares line fit through the maximum amplitudes at each frequency (Figure 9, black line). The purple-colored line indicates the picked peak amplitudes at each frequency within the range of 50–450 Hz, which is the same frequency range as in Figure 8. Amplitudes of less than

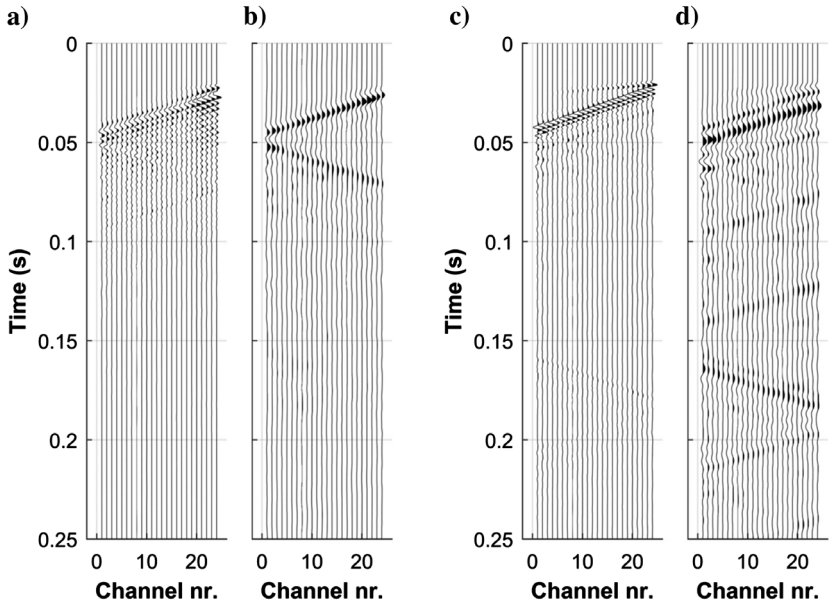

Figure 8. Stacked traces for an active experiment in the shallow well 1, filtered within frequency bands of (a) 50–450 Hz and (b) 0–150 Hz. Stacked traces for an active experiment in the deep well 2, filtered within frequency bands of (c) 50–450 Hz and (d) 0–150 Hz.

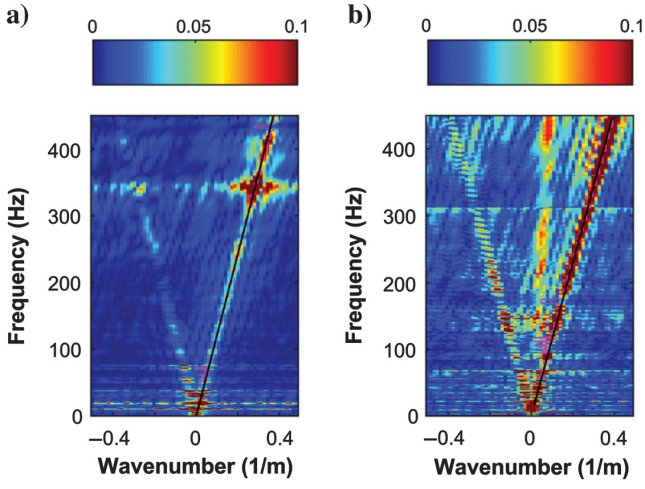

Figure 9. Normalized f-k spectrum of a single shot conducted in (a) the shallow well 1 and (b) the deep well 2. The black line indicates the fitted line for the velocity estimation, and the purple line is the picked maximum amplitude at each frequency.

50 Hz are difficult to pick due to the noise. The frequencies greater than 450 Hz are removed to avoid aliasing because we are limited to wavenumbers smaller than 0.5 m^{-1} due to the hydrophone spacing of 1 m. The second method used to estimate the velocity is the Radon transform. To have the same basis for comparing the results, we band-pass filter the data (50–450 Hz) prior to calculating the Radon transform of the f-k plot. Figure 10 shows the Radon transforms of the events in Figure 9. The tube-wave velocity is estimated from the values of ψ and x' at the bright spot. These maxima in $x' = 0$ and $\psi \approx -3°$ and $\psi \approx 3°$ are the two linear events as sketched in Figure 3. Notice that the Radon transform for the experiment in the deep well shows a second weaker bright spot slightly below $\psi = 0°$, which is interpreted as being the P-wave in the casing (the steeper event in Figure 9b).

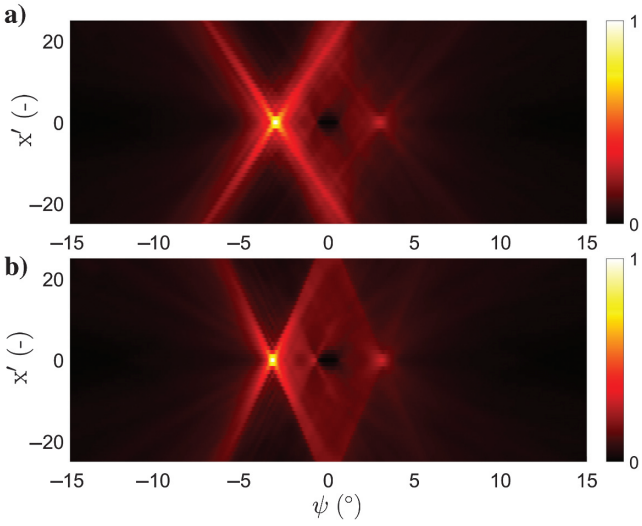

Figure 10. Normalized Radon transform of a single shot conducted in (a) the shallow well 1 and (b) the deep well 2. The maximum amplitude at $x' = 0$ indicates the tube-wave velocity.

Table 2. Results of the tube-wave velocity estimation for different experiments.

	Well	Line fit	Radon
Active (September/17)	1	1208.4 ± 1.7	1198.0 ± 1.4
Active (October/17)	1	1217.6 ± 1.6	1189.0 ± 0.1
Active (March/18) a	1	1217.3 ± 0.6	1217.0 ± 0.1
Active (March/18) b	1	1217.1 ± 1.1	1212.0 ± 0.1
Active (March/18) c	1	1219.0 ± 0.9	1212.0 ± 0.1
Active (March/18) d	1	1220.0 ± 1.6	1215.0 ± 0.1
Active (May/18)	1	1218.0 ± 1.0	1200.0 ± 1.4
Active (October/17)	2	1145.7 ± 0.6	1137.2 ± 1.1
Semipassive (May/18)	1	1216.0 ± 3.8	1213.3 ± 1.2
Passive (October/17)	1	1242.0 ± 11.1	1186.4 ± 1.6
Passive (October/17)	2	1172.0 ± 11.7	1160.0 ± 3.3

Values are in m/s. Well 1 is the shallow borehole, and well 2 is the deep borehole.

The estimated tube-wave velocities for the shallow and deep well are given in Table 2. Figure 11 illustrates the results in well 1. We notice that all results for the active experiments have a very small standard deviation, the largest being ±1.7 m/s for the first test in the shallow well. Approximately 5% of the shots are removed as outliers prior to velocity estimation. The outliers might be caused by inaccuracies in the manually driven hammer source. The velocities computed from the line-fit method for tests 2–4 in the shallow well during October 2017, March 2018, and May 2018 reveal the same velocity, whereas the first experiment (September/17) indicates a velocity that is approximately 7 m/s lower, when the error is taken into account (Figure 11). The experiment in March is repeated three times within 13 days (Table 2: March/18 b, c, d), with nearly the same results for all tests. This demonstrates the repeatability of the method because no changes in the shear modulus within this time period are expected. The velocities computed from the Radon transform are in general lower than those from the line-fit method (Figure 11). In addition, there are more deviations between the results from the Radon transform compared to the line-fit method. We elaborate more on the deviations of both methods in the "Discussion" section. The velocity estimated for the active experiment in the deep well has the highest accuracy, and it is slower than in the shallow well, due to the different borehole geometry. It should be noted that the accuracy is successively lower from the active to the semipassive and passive experiments (Table 2). We also note that the results from the semipassive experiments are comparable with those from the active tests, whereas for the passive measurements the velocities deviate more from the active tests.

Besides the two methods described, traveltime picking of first break and windowed crosscorrelation of events were also tested to estimate the tube-wave velocity, but those methods lead to results with large variations. By using crosscorrelation, the calculated velocities have a standard deviation of approximately 25–40 m/s in the experiments in the shallow well — an order of magnitude worse than the values obtained with the Radon and line-fit methods. We believe that the the reasons for that are twofold. The first reason is the strong "ringing" close to the top of the well, which deteriorates the tube-wave signal in the shallow receivers due to the generation of high-amplitude noise and different wave modes; the

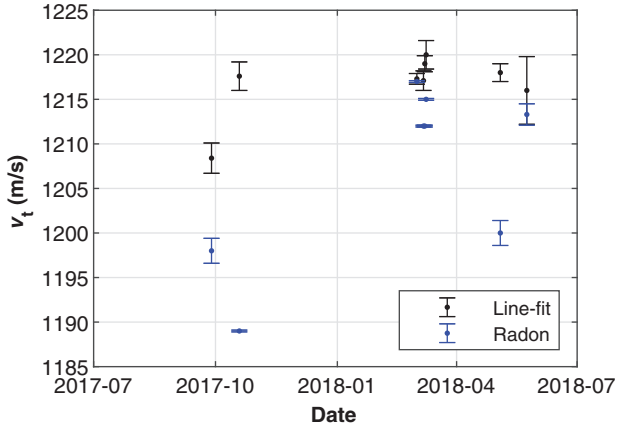

Figure 11. Results of the active and semipassive experiments in well 1 with the standard deviation indicated by the error bars according to Table 2. The standard deviation is calculated from the individual shot, not from stacked data.

DOI:10.1190/geo2020-0294.1

second reason is the reflection at the bottom of the well, which interferes with the data in the deep receivers for the shallow well. This interpretation is reinforced by the fact that interferometry worked better for the bottom half receivers of well 2 (accuracy of approximately 9 m/s), where the bottom well reflections take a longer time to reach the hydrophones.

The line fit in the f-k domain has some drawbacks because amplitudes from other strong events might be picked (Figure 9, the purple line). In our case, this effect is enhanced by the short distance between the first receivers and the source, which causes other wave types to still be strong compared with the tube wave. In general, the f-k domain computations yield the most robust and accurate results when compared with the other methods. Estimations of the tube-wave velocity from passive recordings using slightly different methods are discussed by Borges et al. (2018) and Wehner et al. (2018). We elaborate further on the deviation between the results from the line fit and Radon transform in the "Discussion" section.

S-wave velocity/shear modulus estimation

The promising results for the tube-wave velocity estimation suggest that the formation shear modulus and S-wave velocity could be measured within a reasonable range. Hence, the detection of changes in the shear modulus in the formation might be feasible by measuring the tube-wave velocity.

Although the absolute characterization of the shear modulus in the formation from the measured tube wave is hardly possible, we can check whether consistent results can be achieved from the measurements in both wells. The relation given in equation 4 is used to estimate the shear modulus and S-wave velocity within the formation, using measurements from the active experiments in both wells. For this purpose, we use the results from the line-fit method (see Figure 12). Because the coupling parameter is difficult to measure, we assume $\beta = 0.5$, in between a perfectly coupled and an uncoupled well from the formation. For the velocity estimation, we assume a density value of $\rho_s = 2000\,\mathrm{kg/m^3}$.

We note that the range of the estimated shear modulus μ_S and S-wave velocity V_S from both wells overlap, which is a good sign because the wells are close to each other. The range of the computed V_S in the deep well is smaller due to the lower standard deviation of the measured tube-wave velocity and differing well geometry. From those results, we could estimate a shear modulus of approximately 0.29 GPa and an S-wave velocity of approximately 379 m/s for the formation between 3 and 26 m depth, where the hydrophone array is deployed. We do not have additional measurements of the S-wave velocity at the location of the wells, but several measurements have been conducted in the area around our location (Long and Donohue, 2007; L'Heureux et al., 2013; L'Heureux and Long, 2016). In particular, the Eberg test site (Long and Donohue, 2007), located within a distance of 500–1000 m to the location of the wells, has an estimated S-wave velocity between 120 and 300 m/s for depths to 12 m. This might indicate that our results are in a reasonable range because we are in a similar geologic setting. If the movement of the casing is restricted ($\beta = 0$), the estimated S-wave velocity for our experiments is approximately 280 m/s. We emphasize that the absolute estimation of the formation shear modulus from the measured tube-wave velocity is very difficult to achieve and these results mainly prove the consistency between both wells.

Sensitivity analysis of borehole parameters

To investigate the impact of different borehole geometries and properties, single parameters are varied in the model and compared with the experimental setup in the shallow well (Figure 13).

The diameter of the borehole d_b (Figure 13a) has a relatively significant effect compared to the other parameters. The larger the borehole diameter is, the better the tube-wave monitoring. Exploration and production typical casing diameters of 0.47 m (18 5/8 inch) and 0.34 m (13 3/8 inch) could be used down to depths of 900 and 1700 m, respectively, as shown by Aadnøy (2010). These are larger than the casing diameters in our experimental setup and would be beneficial for the tube-wave velocity estimation. Another important parameter is the casing thickness d_c (Figure 13b). A thinner casing is beneficial for estimating the formation shear modulus because the casing masks the relation between the tube wave and the formation shear modulus (Marzetta and Schoenberg, 1985).

Assuming that the installed tools can be approximated as a cylinder, we calculate the influence of different tool thicknesses $r_{\min}$ (Figure 13c). These might also account for injection pipes or other tools installed in the well. The change in $r_{\min}$ basically leads to a shift of the relation between the tube-wave velocity and the shear modulus, and it has a small effect on the slope compared with the parameters mentioned previously. Installing different tools inside the well would also change the shear modulus μ_t of the tool (Figure 13d). The modeled values cover a wide range of tool materials, but the variation of this parameter also leads only to a shift of the curve.

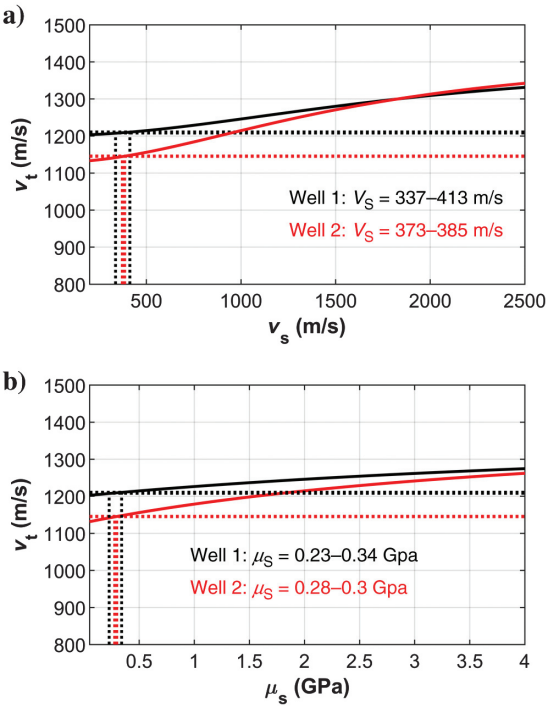

Figure 12. Relation between the tube wave v_t and (a) S-wave velocity V_S and (b) shear modulus μ_S for well 1 (black) and well 2 (red). The horizontal dotted lines indicate the range of the measured tube wave accounting for the measured precision. The vertical dotted lines are the resultant V_S and μ_S range.

We also investigate the effects of the fluid properties. Higher water salinities and fluid pressures can change the bulk modulus K_f (Figure 13e). For temperatures between 2°C and 20°C, the bulk modulus would be within the range from 2.00 to 2.20 GPa. Using the empirical relation from Batzle and Wang (1992), the effect of the fluid temperature is separately plotted in Figure 13f. For our experimental setup in the well, the tube-wave velocity could change approximately 2 m/s for a temperature variation of ±1°C within the fluid. As in the tool radius and shear modulus, we note a shift of the curve due to a different bulk modulus or temperature of the borehole fluid.

The next parameter investigated is the shear modulus of the casing μ_c (Figure 13g), with values above 70 GPa accounting for different steel types. A smaller casing shear modulus facilitates the method, as the slope of the curve becomes steeper for formation shear moduli below 5 GPa. The use of casings made of fiberglass or glass reinforced polyester could decrease the casing shear modulus below 60 GPa (Rafiee, 2013). However, these casings would be limited to a maximum depth of 2000 m and might need a larger casing thickness than conventional steel casings.

The final parameter to be analyzed is β (equation 4), which describes the coupling between the casing and the surrounding formation (Figure 13h). A value of $\beta = 0$ indicates a tight coupling, whereas $\beta = 1$ allows for movement of the casing in the axial direction relative to the formation. The relation between the tube-wave velocity and shear modulus is only influenced for formations in which the shear modulus is low. Although the variations are small, it is important to include it in our analysis. For instance, injected CO_2 close to the well could potentially change the coupling. This would increase the changes in the tube-wave velocity, compared to only accounting for variations of the formation shear modulus.

An important point that needs to be mentioned is that the sensitivity of the tube-wave velocity on the shear modulus is always greater for formations with small initial shear moduli (particularly below 5 GPa), which makes the method most applicable for shallow formations. Therefore, an optimal use of the tube-wave monitoring method might be restricted to specific setups and areas. In addition, the absolute estimation of the shear modulus is a demanding task due to the dependence of the tube wave on several parameters. Hence, the initially estimated shear modulus needs to be verified

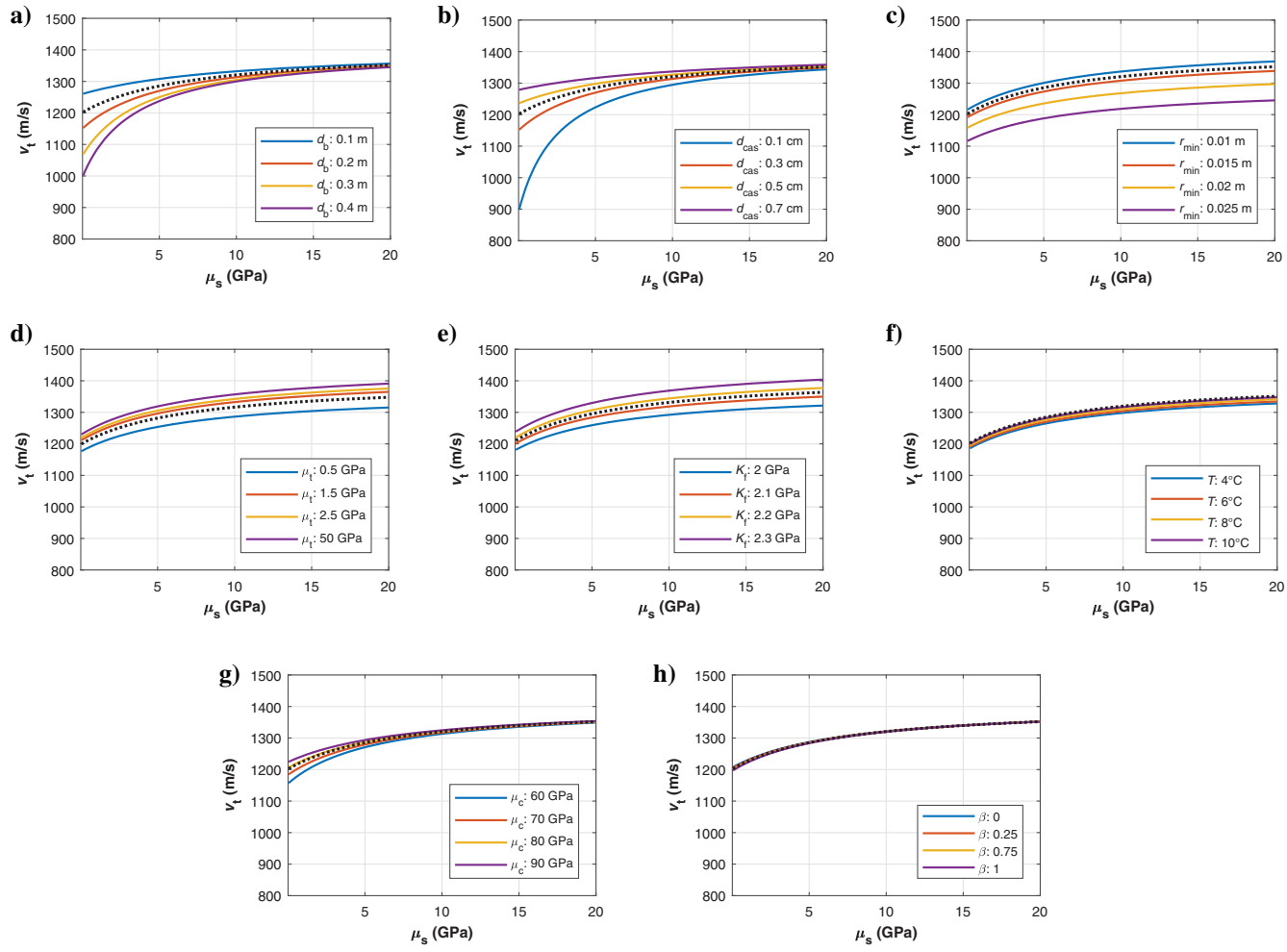

Figure 13. Sensitivity study of the relation between the tube-wave velocity and shear modulus for different parameters. The dotted line indicates the relation for the experimental setup of well 1, the same as in Figure 12 (the black solid line). Each plot illustrates the variation of one parameter with (a) borehole diameter d_b, (b) casing thickness d_c, (c) tool thickness $r_{\min}$, (d) shear modulus of tool μ_t, (e) bulk modulus of borehole fluid K_f, (f) temperature of borehole fluid T, (g) shear modulus of casing μ_c, and (h) coupling between casing and formation β.

DOI:10.1190/geo2020-0294.1

by additional measurements. Monitoring changes within the formation when the baseline status is known, however, could be feasible, assuming that the casing and tool do not change.

DISCUSSION

In this section, we discuss a potential cause for the different results of the active experiments in the shallow well (Table 2). We then elaborate on the variations between the results achieved with the line fit and Radon transform. We also discuss general differences between the active, semipassive, and passive experiments.

For all active measurements in the shallow well, only one significant difference for the results from the line-fit method is noted in the first experiment, with a tube-wave velocity slower by 5–11 m/s (Table 2). Variations for the well casing and tool parameters are very unlikely for the experimental setup. It is not known if shear modulus changes developed within this period, as no other measurements are available. Accounting only for formation changes to explain the difference in the tube wave would reveal a change of $\Delta\mu_S \approx 0.2$ GPa or $\Delta V_S \approx 150$ m/s in the formation. Although these large variations are not likely, shale creep could be an explanation for changes in the geologic formation. Shale creep occurs when the in situ stress in the formation leads to movement of the shale around the borehole (Holt et al., 2020). However, shale creep is demonstrated for consolidated shale from reservoir levels and hence might be quite different for an unconsolidated shallow formation. If we still assume a shale creep effect for low stress levels, the velocity change might be very small in our shallow experiment (less than 1 m/s). Another potential cause for the change in the tube-wave velocity can be variations of the borehole fluid properties. Assuming a 3°C temperature difference in the fluid using the empirical relation of Batzle and Wang (1992), the modeled tube-wave velocity changes by 7 m/s (equation 4). The changes caused by annual variations of the groundwater temperature are expected to be approximately ±2 m/s (Stene et al., 2008), and the minimum temperatures are expected in March and April (Stene et al., 2008), which would contradict our observations. However, the water from the shallow well was pumped out and filled again before the first test due to installation purposes. Therefore, the initial colder borehole fluid temperatures could explain the difference between the experiments. Although the borehole fluid temperature might be the most likely cause of the measured difference between the experiment in September 2017 and all of the other experiments, this cause and the potential shale creep effect are only two explanations, and further investigation of this velocity difference needs to be done. In general, it is strongly recommended to monitor the temperature of the borehole fluid simultaneously with the tube-wave recordings to only retrieve the changes in the formation properties.

The estimated tube-wave velocities from the line-fit and Radon-transform methods both have a small standard variation (Table 2). However, both methods lead to different results and the Radon transform is varying more between each experiment. We note that the values obtained from the Radon transform have almost no deviation from their mean, whereas the line-fit method shows some variance. A possible explanation for the lower standard deviation of Radon velocities is its discrete behavior because a single cell with the maximum amplitude must be chosen for the velocity calculation. Hence, small variations in velocity are not detected, and there is low variability in the result. In contrast to that, the line fit in the f-k domain is computed considering hundreds of points, and small noisy spikes in some specific frequencies create a near-continuous variation around the average value. This hypothesis is confirmed by an analysis of the histograms of the velocities obtained from the Radon transform and f-k methods. The Radon velocities concentrate in about two or three peaks, whereas the line fit follows a normal distribution. This can be observed in more detail in Appendix A.

The consistently lower values for the Radon transform-generated velocities (Figure 11) might be explained by the existence of several different wave modes. Although the event of interest in this work is the tube wave, it is not the only wave mode recorded in the data; there is also an upgoing event (the negative wavenumbers in Figure 9), and a weak downgoing P-wave in the borehole fluid. The upgoing event is the reflected tube wave from the bottom of the well, and it acts as a ghost reflection that creates a notch pattern in the power spectrum (Rosa, 2018). At these notch frequencies, the power spectrum of the tube wave is very weak and the line-fit method recognizes the fluid P-wave as the maximum amplitude. This leads to a bias of the line-fit velocity toward higher values, as $v_{\text{fluid}} > v_t$. To verify this hypothesis, we model two scenarios: one model has only a downgoing tube wave in the well, and in the second model we add a reflected upgoing tube wave and a downgoing fluid wave. Figure 14 shows the f-k transform for the modeled scenarios. We note that the presence of the upgoing wave creates notches and makes the line fit pick some amplitudes from the fluid wave, distorting the velocity calculation.

To compare the velocities obtained in the two modeled scenarios, 100 experiments were simulated. To each experiment, white Gaussian noise was added. The noise intensity was adjusted so that the uncertainty in the line-fit velocity estimation was similar to the values observed in the experimental data. Figure 15 shows the results of these simulations. It can be noticed that the presence of the other wave modes creates a bias on the line-fit velocity toward higher values. In addition, the Radon velocities have a low variability, only moving in "jumps" due to the coarse grid in which they are calculated. We believe that is the explanation on the consistently lower

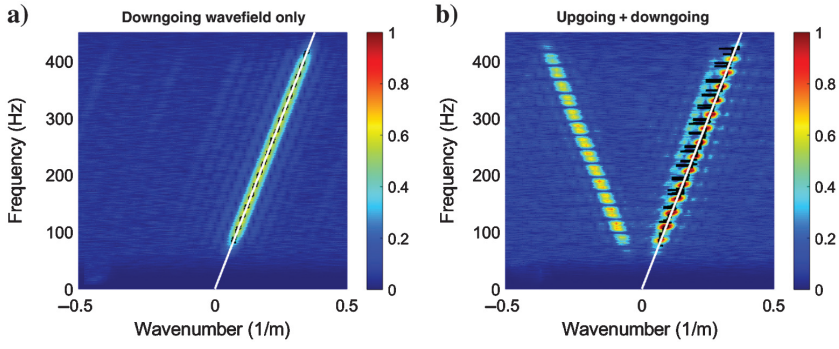

Figure 14. (a) The 2D Fourier transform of the modeled downgoing tube wave. (b) The 2D Fourier transform of the modeled up- and downgoing tube wave, including a downgoing fluid wave. The black lines are the maxima in the f-k domain, and the white line is the best fit of the downgoing event. The color scale is normalized.

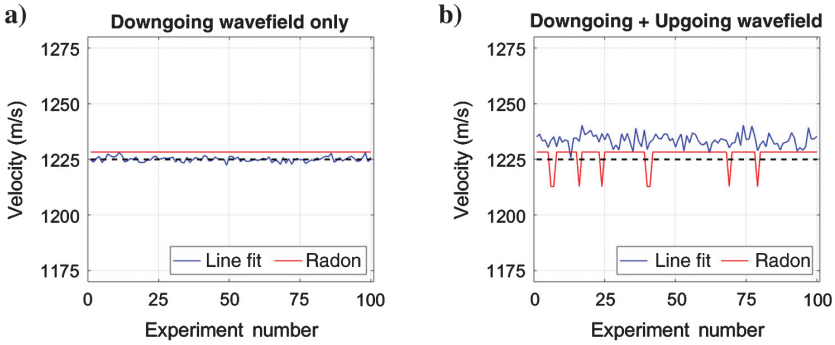

Figure 15. Velocity calculation from the line-fit and Radon transform methods for 100 simulations of the (a) first model (Figure 14a) and (b) second model (Figure 14b), respectively. The black dotted line is the modeled velocity (1225 m/s).

Radon velocities displayed in Table 2. We note that, despite being consistently closer to the "correct" tube-wave velocity, the significant variation in Radon velocities might compromise our ability to use it as a monitoring tool. Hence, the line-fit method appears better suited to monitor trends in tube-wave velocity variations.

Comparing the results from the active and semipassive experiments (Table 2), we note a higher variance in the estimation of the tube-wave velocities in the semipassive data. However, the values obtained for both experiments are within the same range, reinforcing the idea that the active source and the strong background noise can be used as tube wave sources. It should be noted that the main source of energy in the semipassive experiment is further away and noncoherent compared to the active source. In addition, we only use 19 measurements (one measurement equals 24 traces of 4 s) from the semipassive recordings to compute the statistics. Hence, the higher variability in the result is also caused by fewer samples being available. Another observation is that the semipassive recordings are the only experiments where the strongest tube-wave mode is the upgoing one. This is due to the fact that the main energy source in well 2 is located approximately 30 m deeper than the bottom of well 1. As the source is in a different well than the receivers, the generation of Mach waves could be a further explanation for this observation (Wehner et al., 2018) and should be exploited more in future studies. Mach waves are generated from tube waves when the S-wave velocity in the formation is lower than the tube-wave velocity (Meredith, 1990; Meredith et al., 1993). Another application for tube waves and a cross-well setup is reservoir imaging using tube waves that travel through the reservoir (Korneev et al., 2006; Korneev, 2008). In general, passive recordings of the tube wave might be used to detect changes around the well in specific scenarios in which the background noise is strong.

Comparing the active with the full passive experiments, which only recorded noise, we note a large variation and low accuracy for the passive recordings. The tube-wave energy in those recordings is approximately 100 times smaller than in the experiments with an active source, and the velocity estimation becomes more prone to deviations caused by random noise and other wave modes. Monitoring tube-wave changes with this method would require longer observations, to capture a possible trend of formation shear modulus changes. This would imply recording a significant amount of data. For instance, a well with a 100-sensors array would generate roughly 1 TB of raw seismic data per month of continuous monitoring for a 1000 Hz sampling frequency. However, the methodology presented here can be easily automated, without the need of large data storage. Once the data are recorded, filtered, and transformed to the f-k domain, the velocity is calculated, and the seismic data are no longer necessary. A field test of continuous, passive recordings over calendar time, preferably over the course of a year, could reveal the potential for tube-wave monitoring purposes.

CONCLUSION

Measurements of the tube wave in wells carry information of the formation shear modulus and are independent of the formation density. With a simple experimental setup, we found that high-precision measurements of the tube-wave velocity are possible in the f-k domain. The tube-wave velocity is a nonlinear function of many different parameters, making the absolute estimation of the formation properties hardly possible. However, shear modulus and S-wave velocity changes around the borehole could be detected from the tube-wave velocity if a high accuracy of this measurement is achieved. Geologic settings with low initial shear moduli are more sensitive to monitoring with tube-wave velocities and hence are potential application sites. We discuss the effects of well geometry for this potential application, highlighting that larger borehole diameters and thinner casings are beneficial for the method. For monitoring purposes of the geologic formation, it is very important to measure the temperature of the borehole fluid and to correct the estimated formation parameter accordingly. If using an active source, it is recommended to have it located close to the well, to create tube waves with high energy. If a strong background noise source is present at the investigation site, passive recordings could be sufficient. The general idea is that the tube-wave monitoring technique could be used as an initial detection method, locating a depth along the well where changes occur. In a second step, more accurate measurements, e.g., acoustic well logging, can be performed to investigate the detected variations in detail. This could avoid repeated VSP measurements that are costly and have a lower temporal resolution than the tube-wave monitoring. New advances in the use of optical fiber cables for seismic purposes could improve the method, allowing for longer array ranges and finer receiver spacing. The applicability of the method strongly depends on the geology and borehole setup and needs to be checked for each site.

ACKNOWLEDGMENTS

We acknowledge the European Union's Horizon 2020 research and innovation programme under the Marie Skłodowska-Curie grant agreement no. 641943 for the funding of D. Wehner's Ph.D. project within WAVES, and Petróleo Brasileiro S.A. (Petrobras) for the funding of F. Borges's Ph.D. M. Landrø thanks the Norwegian Research Council and the industry partners of the GAMES consortium at NTNU for financial support (grant no. 294404). We would like to acknowledge the technical team at IGP for their support to the experimental setup. A special thanks goes to the editor, J. Shragge, and the four anonymous reviewers for their comments that improved the manuscript significantly.

DATA AND MATERIALS AVAILABILITY

Data associated with this research are available and can be obtained by contacting the corresponding author.

APPENDIX A

DISCRETIZATION OF DATA

A few notes on the discretization are discussed that help to understand potential deviations in the velocity estimation. These points are also of interest for the planning of acquisition setups.

Least-squares line fit

Figure A-1 illustrates the line-fit method in the f-k transform of one of the experiments. The warmer colors represent stronger amplitudes, and no smoothing is applied to the image. The black dots are four points where the maximum amplitudes are extracted. The thick white line is the best least-squares fit to all of the points, and the angular coefficient $\alpha = \tan\theta$ (equation 5) is the estimation for the velocity of the tube wave. Because the number of samples in the frequency domain is significantly larger than in the wavenumber domain due to the differences in time and spatial sampling, several frequency values have the same wavenumber as the maximum (Figure A-1, the magnified box). This is a numerical problem that interferes in the best-fit calculation, and it can be the source of some deviations between the true tube-wave velocity and the value estimated from the angular coefficient. This issue should be considered with respect to the acquisition parameters when the method is tested in field applications.

Radon transform

Figure A-2 shows in more detail the region around the maxima in Figure 10a ($x' = 0, \psi \approx -3°$). The angle for the velocity calculation is picked from the cell with the maximum amplitude in this discrete grid, and every step in the horizontal axis leads to a difference of approximately 2.3 m/s in the tube-wave velocity estimation. That is the reason for the jittery Radon velocities in Figure 15b. This is most likely also the reason why the velocities estimated from Radon transform show a smaller deviation when compared with the line-fit method. The line fit allows for a continuous variation because it is the best fit for hundreds of points, whereas the Radon transform result is a single discrete value that only moves in "steps" of 2.3 m/s, which is above the average deviation from the mean in our experiments. This effect can be seen in the distribution of estimated velocities (Figure A-3): the line-fit velocities show a more continuous, Gaussian-like distribution, whereas the Radon distribution has two strong peaks, with no values between them.

The Radon velocity estimations cannot, in fact, capture small velocity changes, except if the grid for the Radon transform can be made very fine, which significantly increases the time of computation. Still, that alone does not seem to be enough to reproduce the Gaussian behavior observed in the line fit: Figure A-4 shows the mean and standard deviation of one set of experiments (excluding the 5% outliers) as a function of the number of angle steps used in the computation. The processing time is linear on the number of angle steps; e.g., calculation with 10,000 steps

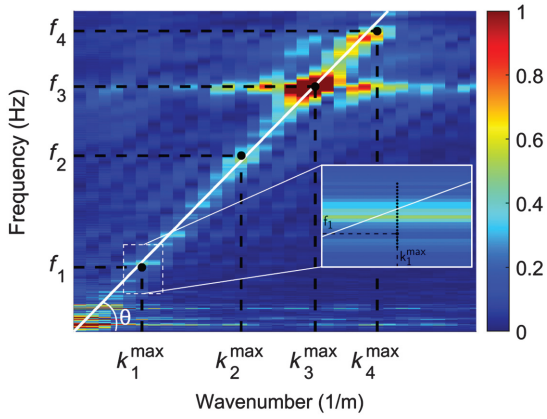

Figure A-1. Normalized discrete f-k spectrum of one active experiment. The thick white line of inclination θ is the best-fit line that goes through (0 m^{-1}, 0 Hz). The magnified box illustrates a magnification on the discrete maximum values.

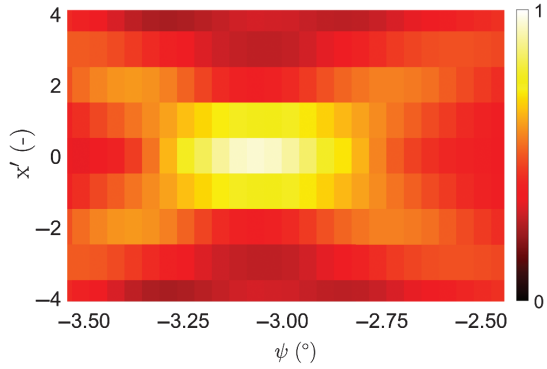

Figure A-2. Magnified view of the Radon transform (Figure 10b), around $x' = 0$, $\psi = -3°$. Note the discretization of the grid.

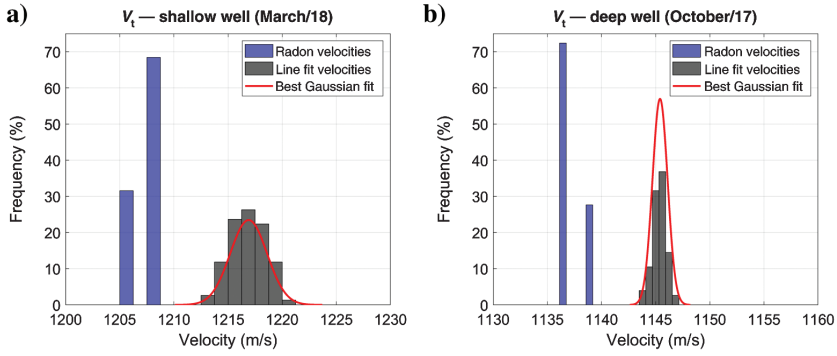

Figure A-3. Histogram of velocities for the line-fit (gray) and Radon (blue) methods, for (a) one experiment in the shallow well and (b) one in the deep well. The vertical axis represents relative frequency of measured tube-wave values. The thick red lines are the Gaussian distributions that best match the line-fit velocities. The distribution for the shallow well (a) has a mean value of $\mu_S = 1216.9$ m/s and standard deviation of $\sigma_S = 1.7$ m/s. For the deep well (b), the values are $\mu_D = 1145.4$ m/s and $\sigma_D = 0.7$ m/s, respectively.

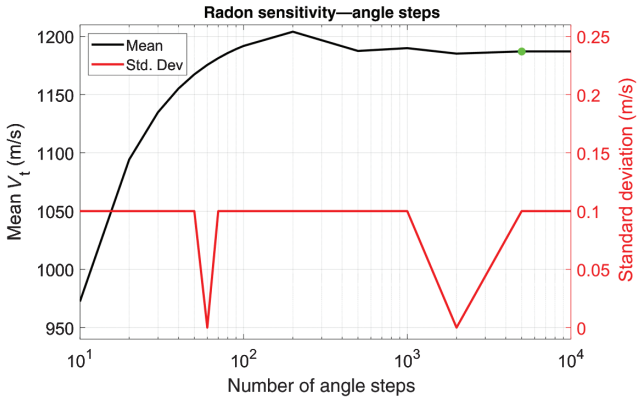

Figure A-4. Sensitivity of velocity calculation with Radon method for different angle steps: mean velocity (black, left *y*-axis) and standard deviation (red, right *y*-axis) for an active experiment in October/17 in the shallow well. Five percent of the points were deemed outliers and have been removed from the statistics. The green dot represents the parameters used for all experiments.

takes 5.0 times longer than with 2000, but it yields a similar result, showing little to no improvement. The green dot represents the values selected for all of the results in this paper (5000), where 1.0 s of data recorded at 0.25 ms sampling (24 channels) takes approximately 30.0 s to process on a conventional desktop computer. Perhaps some preprocessing/data conditioning would be necessary prior to the Radon transform, and this is certainly a point of investigation for our future studies with the method.

REFERENCES

Aadnøy, B. S., 2010, Modern well design: CRC Press.

Batzle, M., and Z. Wang, 1992, Seismic properties of pore fluids: Geophysics, **57**, 1396–1408, doi: 10.1190/1.1443207.

Biot, M. A., 1941, General theory of three-dimensional consolidation: Journal of Applied Physics, **12**, 155–164, doi: 10.1063/1.1712886.

Biot, M. A., 1952, Propagation of elastic waves in a cylindrical bore containing a fluid: Journal of Applied Physics, **23**, 997–1005, doi: 10.1063/1.1702365.

Borges, F., D. Wehner, and M. Landrø, 2018, Calculation of tube wave velocity in a shallow borehole using passive seismic recordings: 80th Annual International Conference and Exhibition, EAGE, Extended Abstracts, ThP403, doi: 10.3997/2214-4609.201801578.

Bussat, S., and S. Kugler, 2011, Offshore ambient-noise surface-wave tomography above 0.1 Hz and its applications: The Leading Edge, **30**, 514–524, doi: 10.1190/1.3589107.

Carcione, J. M., and F. Poletto, 2008, Synthetic logs of multipole sources in boreholes based on the Kelvin–Voigt stress–strain relation: Geophysical Journal International, **174**, 808–814, doi: 10.1111/j.1365-246X.2008.03875.x.

Chang, S. K., H. L. Liu, and D. L. Johnson, 1988, Low-frequency tube waves in permeable rocks: Geophysics, **53**, 519–527, doi: 10.1190/1.1442483.

Claerbout, J. F., 1985, Imaging the earth's interior: Blackwell Scientific Publications.

De Ridder, S., and B. Biondi, 2015, Near-surface Scholte wave velocities at Ekofisk from short noise recordings by seismic noise gradiometry: Geophysical Research Letters, **42**, 7031–7038, doi: 10.1002/2015GL065027.

Dixon, N., D. Russell, and V. Jones, 2005, Engineering properties of municipal solid waste: Geotextiles and Geomembranes, **23**, 205–233, doi: 10.1016/j.geotexmem.2004.11.002.

Ferre, M. C., 1960, Methods and apparatus for exploring earth formations: U.S. Patent 2,924,289 (to Schlumberger Well Surveying Corporation).

Galperin, E. I., 1985, Vertical seismic profiling and its exploration potential: D. Reidel Publishing Company.

Gassmann, F., 1951, Elastic waves through a packing of spheres: Geophysics, **16**, 673–685, doi: 10.1190/1.1437718.

Hardage, B. A., 1981, An examination of tube wave noise in vertical seismic profiling data: Geophysics, **46**, 892–903, doi: 10.1190/1.1441228.

Henriet, J. P., J. Schittekat, and P. H. Heldens, 1983, Borehole seismic profiling and tube wave applications in a dam site investigation: Geophysical Prospecting, **31**, 72–86, doi: 10.1111/j.1365-2478.1983.tb01042.x.

Holt, R., I. Larsen, E. Fjær, and J. Stenebråten, 2020, Comparing mechanical and ultrasonic behaviour of a brittle and a ductile shale: Relevance to prediction of borehole stability and verification of shale barriers: Journal of Petroleum Science and Engineering, **187**, 106746, doi: 10.1016/j.petrol.2019.106746.

Korneev, V. A., 2008, Slow waves in fractures filled with viscous fluid: Geophysics, **73**, no. 1, N1–N7, doi: 10.1190/1.2802174.

Korneev, V. A., A. Bakulin, and S. Ziatdinov, 2006, Tube-wave monitoring of oil fields: 76th Annual International Meeting, SEG, Expanded Abstracts, 374–378, doi: 10.1190/1.2370279.

Kugler, S., T. Bohlen, S. Bussat, and G. Klein, 2005, Variability of Scholte-wave dispersion in shallow-water marine sediments: Journal of Environmental and Engineering Geophysics, **10**, 203–218, doi: 10.2113/JEEG10.2.203.

Kugler, S., T. Bohlen, T. Forbriger, S. Bussat, and G. Klein, 2007, Scholte-wave tomography for shallow-water marine sediments: Geophysical Journal International, **168**, 551–570, doi: 10.1111/j.1365-246X.2006.03233.x.

L'Heureux, J. S., and M. Long, 2016, Correlations between shear wave velocity and geotechnical parameters in Norwegian clays: Proceedings of the 17th Nordic Geotechnical Meeting.

L'Heureux, J. S., M. Long, M. Vanneste, G. Sauvin, L. Hansen, U. Polom, I. Lecomte, J. Dehls, and N. Janbu, 2013, On the prediction of settlement from high-resolution shear-wave reflection seismic data: The Trondheim harbour case study, mid Norway: Engineering Geology, **167**, 72–83, doi: 10.1016/j.enggeo.2013.10.006.

Long, M., and S. Donohue, 2007, In situ shear wave velocity from multichannel analysis of surface waves (MASW) tests at eight Norwegian research sites: Canadian Geotechnical Journal, **44**, 533–544, doi: 10.1139/t07-013.

Marzetta, T. L., and M. Schoenberg, 1985, Tube waves in cased boreholes: 55th Annual International Meeting, SEG, Expanded Abstracts, 34–36, doi: 10.1190/1.1892647.

Meredith, J. A., 1990, Numerical and analytical modelling of downhole seismic sources: The near and far field: Ph.D. thesis, Massachusetts Institute of Technology.

Meredith, J. A., C. H. Cheng, and M. N. Toksöz, 1993, Secondary shear waves from source boreholes: Geophysical Prospecting, **41**, 287–312, doi: 10.1111/j.1365-2478.1993.tb00571.x.

Mordret, A., N. M. Shapiro, and S. Singh, 2014, Seismic noise-based time-lapse monitoring of the Valhall overburden: Geophysical Research Letters, **41**, 4945–4952, doi: 10.1002/2014GL060602.

Norris, A., 1987, The tube wave as a Biot slow wave: Geophysics, **52**, 694–696, doi: 10.1190/1.1442336.

Norris, A. N., 1990, The speed of a tube wave: The Journal of the Acoustical Society of America, **87**, 414–417, doi: 10.1121/1.399262.

Overton, W. C. J., 1957, Shear modulus acoustic well logging: U.S. Patent 2,784,796 (to ExxonMobil Oil Corporation).

Peng, C., J. M. Lee, and M. N. Toksoz, 1996, Pressure in a fluid-filled borehole caused by a seismic source in stratified media: Geophysics, **61**, 43–55, doi: 10.1190/1.1443955.

Radon, J., 1986, On the determination of functions from their integral values along certain manifolds: IEEE Transactions on Medical Imaging, **5**, 170–176, doi: 10.1109/TMI.1986.4307775.

Rafiee, R., 2013, Experimental and theoretical investigations on the failure of filament wound GRP pipes: Composites Part B: Engineering, **45**, 257–267, doi: 10.1016/j.compositesb.2012.04.009.

Rayleigh, L., 1885, On waves propagated along the plane surface of an elastic solid: Proceedings of the London Mathematical Society, **s1-17**, 4–11, doi: 10.1112/plms/s1-17.1.4.

Ringrose, P. S., 2017, Principles of sustainability and physics as a basis for the low-carbon energy transition: Petroleum Geoscience, **23**, 287–297, doi: 10.1144/petgeo2016-060.

Rosa, A. L. R., 2018, The seismic signal and its meaning: SEG.

Schoenberg, M., T. L. Marzetta, J. Aron, and R. P. Porter, 1981, Space-time dependence of acoustic waves in a borehole: The Journal of the Acoustical Society of America, **70**, 1496–1507, doi: 10.1121/1.387107.

Scholte, J., 1942, On the Stoneley wave equation: Proceedings of the Koninklijke Nederlandse Akademie van Wetenschappen, **45**, 20–25.

Scholte, J., 1947, The range of existence of Rayleigh and Stoneley waves: Geophysical Journal International, **5**, 120–126, doi: 10.1111/j.1365-246X.1947.tb00347.x.

Stene, J., K. Midttömme, H. Skarphagen, and B. G. Borgnes, 2008, Design and operation of ground-source heat pump systems for heating and cooling of non-residential buildings: 9th International Energy Agency Heat Pump Conference.

Stevens, J. L., and S. M. Day, 1986, Shear velocity logging in slow formations using the Stoneley wave: Geophysics, **51**, 137–147, doi: 10.1190/1.1442027.

Stoneley, R., 1924, Elastic waves at the surface of separation of two solids: Proceedings of the Royal Society of London: Series A, Containing Papers of a Mathematical and Physical Character, **106**, 416–428, doi: 10.1098/rspa.1924.0079.

Troncoso, J. H., and E. Garcés, 2000, Ageing effects in the shear modulus of soils: Soil Dynamics and Earthquake Engineering, **19**, 595–601, doi: 10.1016/S0267-7261(00)00066-X.

Wehner, D., F. Borges, and M. Landrø, 2018, Using well operation noise to estimate shear modulus changes from measured tube waves — A feasibility study: Fifth CO2 Geological Storage Workshop, EAGE, FrCO204.

White, J. E., 1965, Seismic waves: Radiation, transmission, and attenuation: McGraw-Hill Book Company.

Winkler, K. W., H. L. Liu, and D. L. Johnson, 1989, Permeability and borehole Stoneley waves: Comparison between experiment and theory: Geophysics, **54**, 66–75, doi: 10.1190/1.1442578.

Biographies and photographs of the authors are not available.

DOI:10.1190/geo2020-0294.1